# ANALYZING THE RELATIONSHIP BETWEEN LAND COVER AND LAND SURFACE TEMPERATURE (LST) DISTRIBUTION IN THE MOUNT PAPANDAYAN AREA, WEST JAVA

Tin Widyani Satriawan (1), Endah Sulistyawati (2), Agung Budi Harto (3)

[1] Undergraduate Program in Biology, Institut Teknologi Bandung, Jl. Ganesha No. 10, Bandung 40132, Indonesia
[2] School of Life Sciences and Technology, Institut Teknologi Bandung, Jl. Ganesha No. 10, Bandung 40132, Indonesia
[3] Faculty of Earth Sciences and Technology, Institut Teknologi Bandung, Jl. Ganesha No. 10, Bandung 40132, Indonesia
Email: tinsatriawan@gmail.com; endah@sith.itb.ac.id; agung@gd.itb.ac.id

**KEYWORDS:** OBIA, topographic correction, Landsat, LSE

**ABSTRACT** Land surface temperature (LST) is an essential indicator for detecting climate change due to its role in providing information regarding the energy balance process on the earth's surface. In understanding the climate process of an area, it is important to study the influence of land cover on LST. However, over mountainous areas, such studies are limited mostly because of the strong effect of topography on LST. In this study, the relationship between land cover and LST distribution in the Mount Papandayan area, West Java, Indonesia was analyzed using Landsat 8 OLI/TIRS imagery. To estimate LST, single-channel algorithm and land surface emissivity (LSE) correction through NDVI-based method (NBEM) were used. The effect of topography on LST was then normalized using a multi-linear regression model from digital elevation model (DEM) and solar irradiance. Land cover classification was done using object-based image analysis (OBIA) through multi-resolution segmentation and threshold classification combined with nearest neighbor (NN) classification. The results reveal that the effect of topography on LST was reduced after correction. LST in the Mount Papandayan area ranged from 14.27 to 40.01°C with a mean value of 23.77°C. The distribution of mean LST across land cover types was found to be the highest in crater area (29.59°C), followed by built-up (26.91°C), cropland (25.64°C), tea plantation (24.16°C), pasture (23.56°C), shrub (22.40°C), and forest area (20.63°C). The difference between the mean LST of each land cover and the mean LST of the whole study area indicates the heating or the cooling effect of each land cover type on the area. By using the mean LST of the study area as the reference LST, it can be inferred that crater, built-up, cropland, and tea plantation land cover types contribute to heating the area, whereas pasture, shrub, and forest area contribute to cooling the area. From this study, it can be concluded that in the Mount Papandayan area, the distribution of LST across land cover types was the highest in crater, followed by built-up, cropland, tea plantation, pasture, shrub, and forest.

## 1 INTRODUCTION

Land surface temperature (LST) is a thermal infrared remote sensing product which displays the kinetic temperature of the surface of the earth from the satellite's sensor point of view. Thermal infrared remote sensing deals with data that are acquired in the thermal infrared (TIR) domain of the electromagnetic spectrum. In most cases, the wavelength in which TIR radiation of the earth is measured ranges between 3-5 μm and 8-14 μm due to atmospheric window (Sabins, 2007). LST retrieval using remote sensing is possible because every object that has a kinetic temperature above 0 K (273 ˚C) emits electromagnetic radiation. With a kinetic temperature around 300 K, earth emits electromagnetic radiation that peaks in the TIR domain (Kuenzer & Dech, 2013; Sabins, 2007). As a measurement of how cold or hot the surface of the earth is, LST provides information regarding energy exchange between land and atmosphere. Due to its importance in the surface-atmosphere system, LST is specified as one of the essential climate variables (ECVs) by the Global Climate Observing System (GCOS, 2016).

In the last few decades, land cover conversion from vegetated area to impervious area is known to cause an increase in LST (Mallick *et al*., 2008). A rise in LST above a certain point can have an adverse impact on air quality, hydrology, carbon cycle, and biodiversity. In its association with air quality, high LST can result in the mixing of pollutants in the layer of air near the land surface, thus exacerbating pollution (Rao, 2014). In addition, surface heating drives the increase of air temperature and humidity (Pleim & McKeen, 2012). The warmer the air temperature is, the greater the amount of water vapor the air can hold. This can affect hydrologic cycles in terms of precipitation, soil moisture, water storage and run off (Stagl *et al*., 2014). Concerning the carbon cycle, higher LST is found to drive up carbon emissions into the atmosphere through the increase of soil respiration (Dilekoğlu & Sakin, 2017). More importantly, for biodiversity, a significant rise in LST can lead to a shift in the community composition, given that each species has different ability in adapting to environmental changes (Hannah *et al*., 2005).

Previous studies on the influence of land cover on LST have been attempted through different approaches to gain a deeper understanding of the climate process of an area. It is found that LST depends on surface land cover properties, such as the ability of a land cover to absorb solar radiation, heat and perform evapotranspiration (Bonan, 2016; Mallick *et al*., 2008). Across different regions, studies reported that LST is found to be higher in built-up areas, followed by bare soil, sparsely vegetated areas, and densely vegetated areas (Feizizadeh *et al.*, 2012; Mbithi *et al*., 2013; Sun *et al*., 2012) Although such studies are common, few are done over mountainous areas due to the strong effect of topography on LST. In this study, the relationship between land cover and LST distribution in the Mount Papandayan area, West Java, Indonesia was analyzed using Landsat 8 OLI/TIRS imagery.

## 2 STUDY AREA

This study was done in the Mount Papandayan area of West Java, Indonesia which includes the tropical mountain forests of Mount Papandayan Nature Reserve, some parts of Kamojang Nature Reserve and the surrounding region (7.109-7.378 S, 107.660-107.824 E) (Figure 1). Mount Papandayan Nature Reserve is located in the center of the study area, observable as an elongated-shaped forest patch that extends from north to south. To the north lies the Kamojang Nature Reserve forest patch that stretches from east to west. Elevation within the area ranges from 877.4 to 2649.5 masl with complex topography involving steep, hilly, mountainous regions. The Mount Papandayan area is classified as type B climate according to Schmidt and Ferguson classification system due to its annual rainfall and humidity that varies from 2500-3000 mm per year and 70-80% respectively (BBKSDA Jabar, 2016).

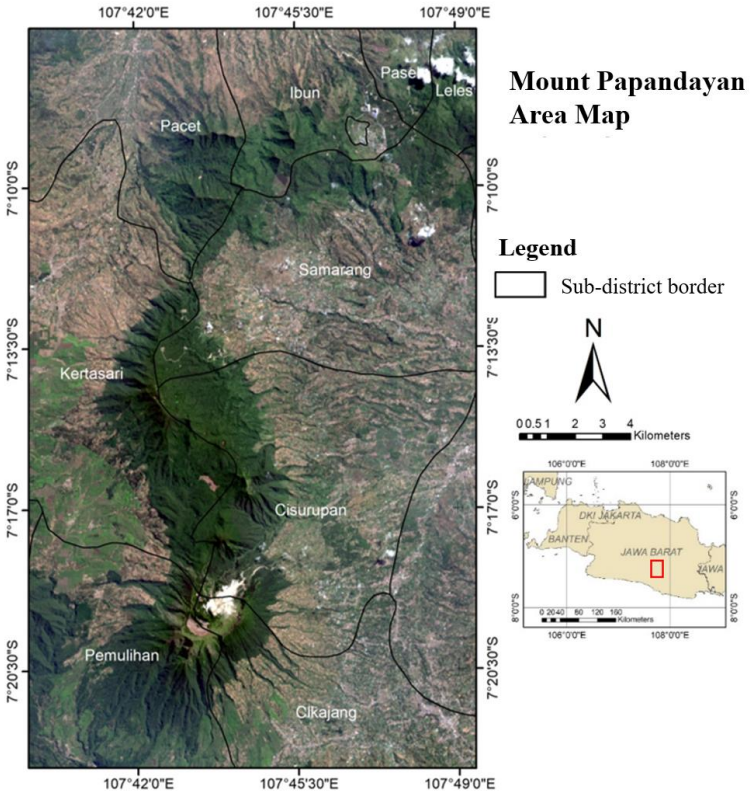


**Figure 1** Map of the study area


## 3 MATERIALS

### 3.1 Remote Sensing Data

The main data used in this study is Landsat 8 OLI/TIRS satellite imagery acquired on August 16, 2018. Preprocessing including atmospheric and topographic correction was done for band 1 to band 7 using the ATCOR3 module in ERDAS IMAGINE 2014. Other supporting data used are Indonesia's official contour and road vectors issued by Badan Informasi Geospasial. The digital elevation model (DEM) was generated from the contour vector.

### 3.2 Field Data

In situ observation was done to obtain ground truth points in March 2019. Data taken were coordinate locations using Garmin GPS receiver 62S, photos, and land cover descriptions. To facilitate data collection, an Android application called Open Data Kit (ODK) Collect was used.

## 4 METHODOLOGY

### 4.1 Land Surface Temperature (LST) Retrieval

LST retrieval in this study was carried out using the raster calculator tool in ArcMap 10.4. The general steps covered land surface emissivity (LSE) estimation, radiometric correction for Landsat TIRS data, LST estimation using single-channel algorithm from known LSE and topographic correction for LST. Workflow for LST retrieval is shown in Figure 2.

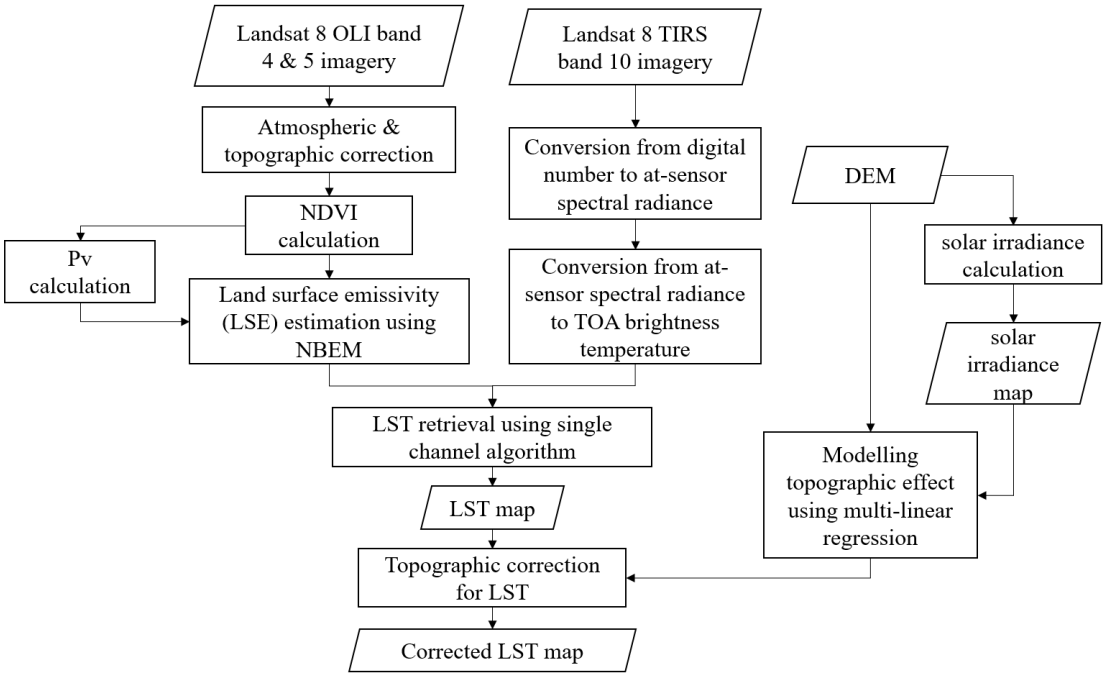


**Figure 2** Workflow for LST retrieval

LSE is an important parameter for surface characterization in LST retrieval. Here, LSE estimation was done using normalized difference vegetation index or NDVI-based method (NBEM). As the term suggests, the method is based on the statistical relationship between NDVI and LSE (Sobrino *et al*., 2008; Tang & Li, 2014). LSE was calculated using Equation (1), as written below,

$$\varepsilon_\lambda = \begin{cases} \varepsilon_{s\lambda}, & NDVI < NDVI_s \\ \varepsilon_{v\lambda} P_v + \varepsilon_{s\lambda}(1 - P_v), & NDVI_s \leq NDVI < NDVI_v \\ \varepsilon_{v\lambda}, & NDVI > NDVI_v \end{cases} \quad (1)$$

where $\varepsilon_{s\lambda}$ is soil emissivity (0,9668), $\varepsilon_{v\lambda}$ is vegetation emissivity (0,985), $NDVI_S$ is the NDVI value of a pixel which consisted only of bare soil (0,1) and $NDVI_V$ is the NDVI value of a fully vegetated pixel (0,8) (Jiménez-muñoz *et al.*, 2009; Carlson & Ripley, 1997). NDVI and proportion of vegetation (Pv) were calculated using Equation 2 and Equation (3) (Carlson & Ripley, 1997) as follows,

$$NDVI = \frac{band\ 5\ (NIR)\ - band\ 4\ (Red)}{band\ 5\ (NIR) + band\ 4\ (Red)} \quad (2)$$

$$Pv = \left(\frac{NDVI\ - NDVI_s}{NDVI_v\ - NDVI_s}\right)^2 \quad (3)$$

From the known LSE value, LST can be estimated. The method chosen for LST retrieval depends on the number of thermal infrared band available. Landsat 8 TIRS has two thermal infrared bands, which are band 10 and band 11. However, since 2014 USGS suggested discontinuing the use of band 11 for split-window algorithm in LST retrieval due to calibration error (USGS, 2017). For that reason, this study utilized band 10 (10.6-11.19 µm) for LST retrieval using single-channel algorithm developed by Jiménez-muñoz *et al*. (2009).

Before calculating the LST, radiometric correction had to be applied first to band 10 imagery by converting digital number to at-sensor spectral radiance or $L_\lambda$ (Equation 4) and $L_\lambda$ to top of atmosphere brightness temperature or BT (Equation 5) as follows,

$$L_\lambda = M_L \times Q_{cal} + A_L \tag{4}$$

$$BT = \frac{K_2}{\ln\left(\frac{K_1}{L_\lambda} - 1\right)} - 273{,}15 \tag{5}$$

where $Q_{cal}$ is band 10 digital number, $M_L$ is band-specific multiplicative rescaling factor, $A_L$ is band-specific additive rescaling factor, $K_1$ and $K_2$ are band 10 thermal constants. The values for $M_L, A_L, K_1$ and $K_2$ can be found in the imagery's metadata file (USGS, 2019).

After radiometric correction for band 10 was done, LST was calculated using single-channel algorithm (Jiménez-muñoz *et al.*, 2009) through Equation 6 as follows,

$$T_0 = \gamma\left(\frac{\psi_1 L_\lambda + \psi_2}{\varepsilon_\lambda} + \psi_3\right) + \delta \tag{6}$$

where $T_0$ is LST (˚C) before topographic correction. Parameters $\gamma$ and $\delta$ were estimated using Equation 7-8, while atmospheric functions $\psi_1$, $\psi_2$, and $\psi_3$ were estimated using Equation 9-11 radiation (Jiménez-muñoz *et al*., 2009), respectively,

$$\gamma = \frac{BT^2}{1{,}324\, L_\lambda} \tag{7}$$

$$\delta = BT - \frac{BT^2}{1{,}324} \tag{8}$$

$$\psi_1 = \frac{1}{\tau} \tag{9}$$

$$\psi_2 = -L_d - \frac{L_u}{\tau} \tag{10}$$

$$\psi_3 = L_d \tag{11}$$

where $\tau$ is atmospheric transmission, $L_u$ is upwelling radiation, and $L_d$ is downwelling estimated using Atmospheric Correction Parameter Calculator (Barsi *et al.*, 2003).

Last, topographic correction had to be done to minimize the effect of topography on LST. This step is important, especially because the study area contains mountainous region. Using Equation 12 which is modified from Malbéteau *et al*. (2017), LST was estimated as follows,

$$T_{corr} = T_0 - 0{,}4(T_{ML} - \overline{T_{ML}}) \tag{12}$$

where $T_{corr}$ is LST after correction, $T_{ML}$ is LST simulated from topography effects, and $\overline{T_{ML}}$ is the average of LST simulated from topography effects. Modification was done by adding 0.4 as a constant for $T_{ML} - \overline{T_{ML}}$ which means that for this study area, only 40% of the topography effect was corrected. $T_{ML}$ was calculated using Equation 13 (Malbéteau *et al.*, 2017) as written below,

$$T_{ML} = \overline{T_0} + A_E(E - \bar{E}) + A_{Rg}(Rg - \overline{Rg}) \tag{13}$$

Where E is elevation from DEM, $Rg$ is solar irradiance in kW/m$^2$, $A_E$ and $A_{Rg}$ is multi-linear regression coefficient for elevation and solar irradiance. Solar irradiance ($Rg$) was estimated using the area solar radiation tool in ArcMap 10.4.1 by dividing solar radiation raster with duration raster.

### 4.2 Land Cover Classification

For classification purpose, Mount Papandayan area was categorized into seven land cover classes, which are forest, shrub, pasture, tea plantation, cropland, built-up, crater, and water body (Table 1). The selection of these land cover classes was adapted from the study done by Primajati *et al*. (2011) in the same region. To carry out the classification using object-based image analysis (OBIA), eCognition Developer software was used. The steps included segmentation, a combination of threshold and nearest neighbor (NN) classification and manual editing.

**Table 1** Land cover class description

| Land Cover Class | Description |
|---|---|
| Forest | Areas dominated by trees |
| Shrub | Areas covered by shrub, herbaceous plants, and sparsely arranged trees |
| Pasture | Areas dominated by grass |
| Tea plantation | Areas dominated by tree plantation |
| Cropland | Uncultivated and cultivated agricultural land, including paddy fields |
| Built-up | Areas covered by buildings and roads |
| Crater | Depression area in the form of open land covered by sulfur sediment, rocks, and bare soil caused by volcanic activity |
| Water body | Areas covered by water, such as lake and pond |

The first step in land cover classification using OBIA was segmentation. Here, multi-resolution segmentation was employed to Landsat 8 OLI imagery band 1, 2, 3, 4, 5, 6, and 7. Parameters applied were set to 30 for scale, 0.02 for shape, and 0.5 for compactness.

The segmented objects were then classified into forest, shrub, tea plantation, cropland, built-up, cloud, and water body using the classification scheme depicted in Figure 3. Classifiers used here were nearest neighbor (NN) and threshold classifier. NN classifier used training samples and defined feature spaces to classify the objects. To determine which feature spaces or bands were best for NN classification in each step, feature space optimization was applied. For threshold classification or fuzzy membership function classification, the user's expert knowledge was used to classify the objects by defining rules and thresholds. Here, the classification was done through several intermediate land cover classes which later were classified or re-assigned to the final land cover classes, excluding pasture and crater. Refinement using NN, threshold, and manual classification was also performed for incorrectly classified objects. Lastly, due to their specificity and locality, pasture and crater classes were classified manually.

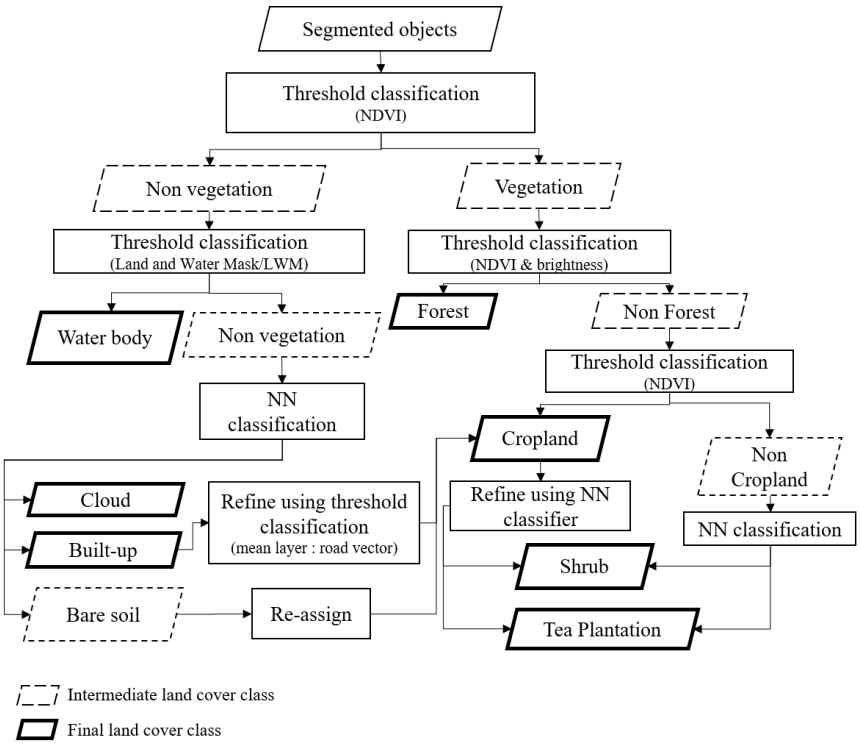


**Figure 3** Classification scheme used for classifying forest, shrub, tea plantation, cropland, built-up, cloud, and water body

The resulting land cover map was then validated using accuracy assessment based on the ground truth data. The ground truth data were obtained from field observation conducted in March 2019 and high-resolution imagery from Google Earth (2019) taken in 2018. Due to difficult terrain in the field, ground truth points were chosen using stratified random sampling combined with occasional sampling. A total of 288 ground truth points were then used to create an error matrix. From the error matrix, producer's accuracy, user's accuracy, overall accuracy, and Kappa statistic were calculated.

### 4.3 Data analysis

To analyze the relationship between land cover and LST distribution, values of each pixel from LST map and land cover map were extracted. Statistical analysis was then done in SPSS Statistics 25. Kolmogorov-Smirnov normality test was used to check the data distribution. Kruskal-Wallis test and post hoc test were then applied to the non-normal data to analyze whether the average LST of each land cover differs significantly.

## 5 RESULT AND DISCUSSION

### 5.1 LST Retrieval

Mount Papandayan LST map before and after topographic correction is shown in Figure 4. There are several ways to evaluate the effectiveness of topographic correction for LST. One of them is through visual observation. Before topographic correction (Figure 4a), it can be seen that the east-facing slope of the mountain ridge (depicted by the black arrow) that is exposed to the sun has a higher LST than the west-facing shaded slope. After topographic correction (Figure 4b), no contrasting LST difference is visually observed from either side of the mountain ridge.

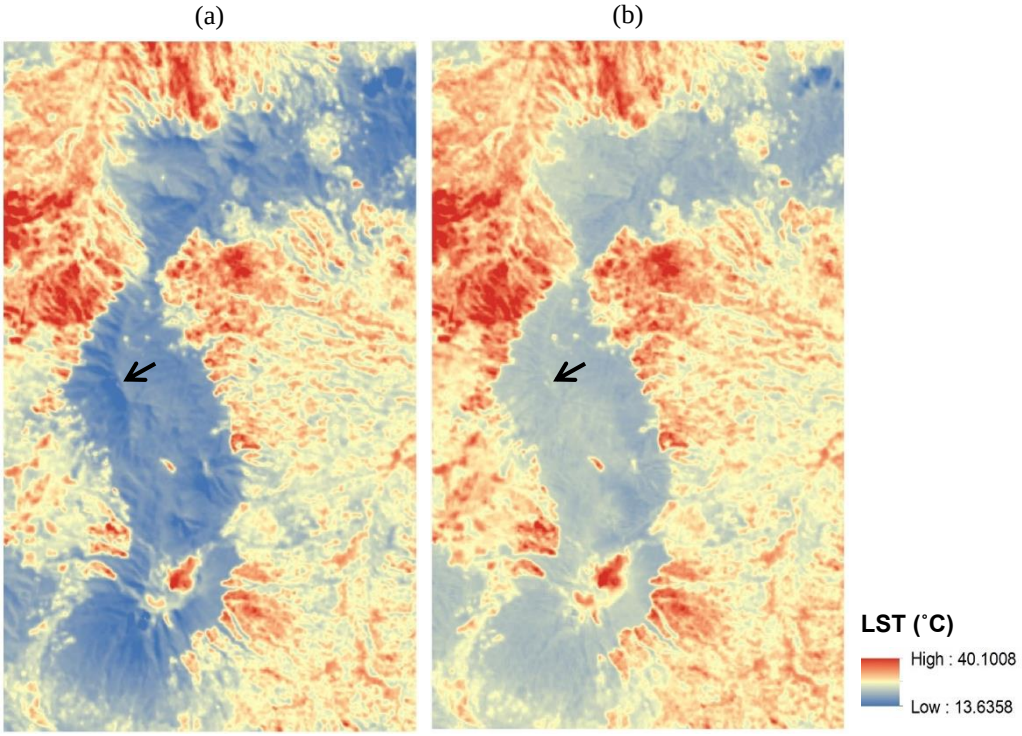


**Figure 4** Mount Papandayan LST map (a) before topographic correction (b) after topographic correction

Considering that the aim of topographic correction is to minimize the effects of topography by estimating the LST that would be observed on flat terrain (Malbéteau *et al.*, 2017), LST for lower elevations is expected to decrease and LST for higher elevations is expected to increase. Therefore, after topographic correction, LST range and standard deviation become narrower as shown in the summary statistics of Mount Papandayan area's LST (Table 2). This phenomenon can also be observed visually in Figure 4, where the formerly dark blue-colored mountain (Figure 4a) becomes light-colored after topographic correction (Figure 4b).

Aside from visual observation, the success of topographic correction can be evaluated by analyzing the correlation

between LST and topographic parameters. Here, the topographic parameter taken into account is solar irradiance (Zhang & Gao, 2011 in Malbéteau *et al.*, 2017). After correction, the correlation coefficient between LST and solar irradiance drops from 0.32 to 0.22, suggesting that the topography effect is successfully minimized.

**Table 2** Summary statistics of Mount Papandayan area's LST before and after topographic correction

| Statistics | LST Before Topographic Correction (˚C) | LST After Topographic Correction (˚C) |
|---|---|---|
| Minimum LST | 13.64 | 14.27 |
| Maximum LST | 40.10 | 40.01 |
| Average LST | 23.77 | 23.77 |
| Standard Deviation LST | 3.69 | 3.23 |
| Correlation coefficient between LST and solar irradiance | 0.32 | 0.22 |

### 5.2 Land Cover Classification

Land cover classification result for Mount Papandayan can be seen in Figure 5. From the accuracy assessment, an overall accuracy of 79.9% was obtained. According to Loveland et al. (2005), an overall classification accuracy of around 75% is common for a large study area, especially when done with non-manual interpretation. Aside from the size of the area being mapped and the method employed, accuracy is also greatly influenced by the number of classes used. To further justify the result, Kappa statistic was calculated. A value of 0.75 was obtained, indicating that the land cover map is considered as substantial following the categorization by Landis and Koch (1977). The total area mapped is 51196.41 ha. Most of the area belongs to cropland (24623.73 ha) and forest (14974.74 ha). The rest is composed of shrub (4806 ha), tea plantation (4035.06 ha), built-up (2136.87 ha), pasture (485.91 ha), crater (124.92 ha) and water body (9.18 ha).

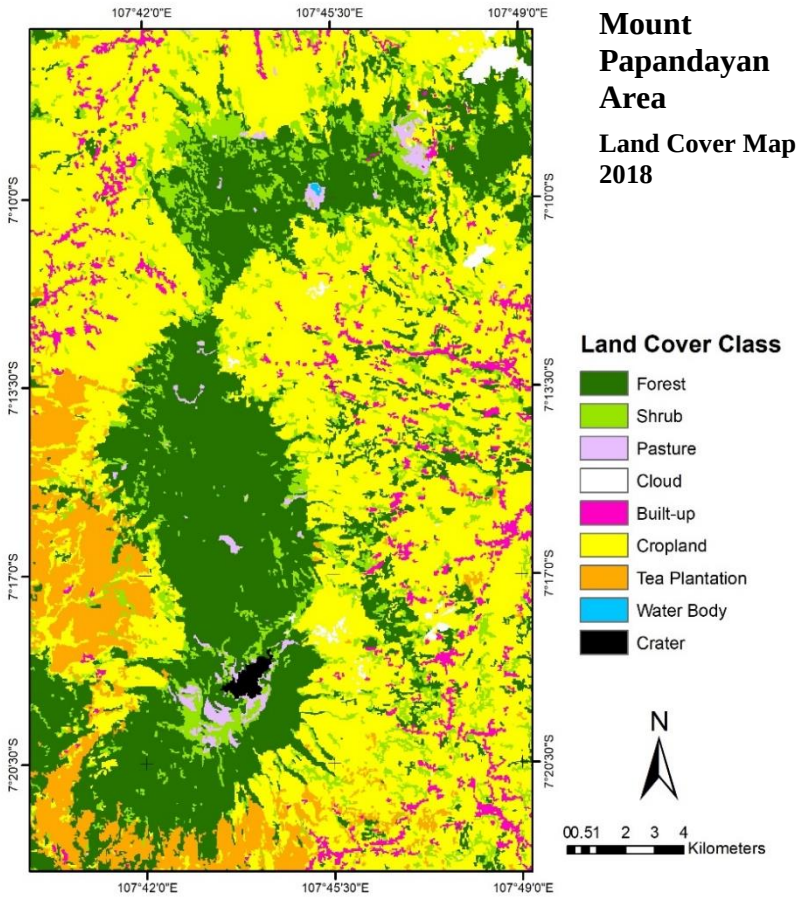


**Figure 5** Land cover map of Mount Papandayan Area

### 5.3 Relationship between Land Cover and LST

Figure 6 demonstrates the LST distribution across land cover classes. From the statistical analysis, it is known that the average LST of each land cover differs significantly from one another. Average LST from the lowest to the highest belongs to forest, shrub, pasture, tea plantation, cropland, built-up and crater, respectively. A similar pattern is also observed in previous researches concerning the influence of LST on land cover in forest or densely vegetated land, pasture, cropland, and impervious land (Hua & Ping, 2018; Latif & Kamsan, 2017; Sun *et al.*, 2012).

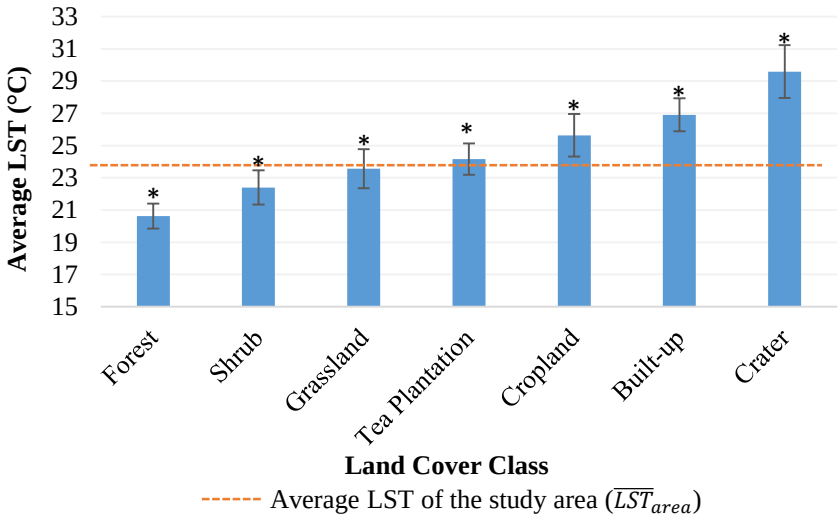


**Figure 6** LST distribution for each land cover class (* significant differences $p < 0.05$)

In addition to exhibiting the pattern of LST for each land cover class, Figure 6 also demonstrates the comparison between the average LST of each class ($\overline{LST}$) and the average LST of the whole study area ($\overline{LST}_{area}$), excluding water body class. According to Zhou & Cao (2019), by treating $\overline{LST}_{area}$ as the reference LST, the contribution of each land cover class to heating or cooling of the area can be calculated. In Table 3, LST reduction or cooling effect of a land cover class compared to $\overline{LST}_{area}$ is indicated by the negative value of $\overline{LST}$-$\overline{LST}_{area}$. Conversely, LST increase or heating effect of a land cover compared to $\overline{LST}_{area}$ is specified by the positive value of $\overline{LST}$-$\overline{LST}_{area}$. Therefore, forest, shrub, and pasture are the source of cooling in the study area, while cropland, built-up, and crater are the source of heating.

**Table 3** LST statistics of each land cover along with LST reduction compared to average LST of the study area

| Land Cover Class | $\overline{LST}$ (°C) | Min LST (°C) | Max LST (°C) | SD LST (°C) | $\overline{LST}$-$\overline{LST}_{area}$ (°C) |
|---|---|---|---|---|---|
| Forest | 20.63 | 14.97 | 35.71 | 1.56 | -3.17 |
| Shrub | 22.40 | 14.88 | 36.17 | 2.14 | -1.39 |
| Pasture | 23.56 | 18.28 | 32.96 | 2.41 | -0.23 |
| Tea Plantation | 24.16 | 19.31 | 34.71 | 1.96 | 0.37 |
| Cropland | 25.64 | 17.37 | 40.01 | 2.64 | 1.84 |
| Built-up | 26.91 | 18.97 | 38.56 | 2.05 | 3.11 |
| Crater | 29.59 | 19.09 | 35.87 | 3.27 | 5.80 |

Forest has the lowest LST of all the other classes. Several factors that play an important part in generating low LST in forest are high rate of evapotranspiration and high turbulence. Evapotranspiration in forest is composed of transpiration from the tree canopy, canopy interception and barely of soil evaporation. Evapotranspiration reduces LST by releasing latent heat from forest surface to the atmosphere. Furthermore, forest has high turbulence due to high surface roughness caused by the height and density of the tree canopy. Turbulence carries air and heat resulting from the release of latent heat and sensible heat away from the forest surface (Bonan, 2016).

Similar to forest, average LST of other vegetated land cover classes such as shrub, pasture, and tea plantation are affected by evapotranspiration and turbulence. For areas with low vegetation density, evapotranspiration is known to

be lower than those with high vegetation density (Wang *et al.*, 2018). The same goes for turbulence, which decreases as canopy height declines (Bonan, 2016). These factors explain why shrub has lower LST compares to pasture and tea plantation. Specifically, in the study area, pasture is cooler than tea plantation presumably because of its spatial arrangement. Pasture patches in Mount Papandayan area are relatively small in size and distributed inside forests, causing it to be highly impacted by the cooling effect of forest.

Cropland has a comparatively high LST with a wide range and high standard deviation. This wide range of LST is influenced by the heterogeneity of vegetation density in cropland class that includes both uncultivated and cultivated land. LST of uncultivated cropland is in contrast to that of cultivated cropland. Uncultivated cropland in the form of bare field has low evapotranspiration and turbulence, resulting in higher LST (Bonan, 2016).

In the study region, built-up class serves as a contributor of heating. Slightly different from vegetated areas, here albedo plays an important role in increasing the LST. Asphalt roads and dark-roofed buildings have low albedo that causes them to absorb most of the incoming energy and accumulate heat. Conversely, for bright-colored roofs and roads, albedo does not count as the source of heating (Forman, 2014). In the Mount Papandayan area, most of the settlements have clay roofs, which are known to have a cooling effect (Lesado & James, 2018). However, hydrocarbon and aerosol pollution produced from human activity often darken road and roof surfaces, thereby increasing their albedo and LST. Furthermore, built-up land cover tends to have less vegetated and bare soil areas, causing less latent heat from evapotranspiration escaping from the surfaces (Forman, 2014).

Crater has the highest LST among other classes. Mount Papandayan's crater area is mostly covered by sulfur sediment, rocks and bare soil with scarce vegetation stands. This results in low evapotranspiration and high LST. Moreover, there are several fumaroles scattered in the crater area. These fumaroles have temperatures ranging from 200 to 280˚C according to Badan Geologi Kementerian ESDM (2016).

## 6 CONCLUSIONS

This research analyzed the relationship between land cover and land surface temperature (LST) in Mount Papandayan Area, West Java, Indonesia using Landsat 8 OLI/TIRS imagery. Topographic correction for LST is considered as successful, resulting in LST ranging between 14.27 and 40.01°C with a mean value of 23.77°C. LST was found to be the highest in crater area (29.59°C), followed by built-up (26.91°C), cropland (25.64°C), tea plantation (24.16°C), pasture (23.56°C), shrub (22.40°C), and forest area (20.63°C). By using the mean LST of the study area as a reference LST, it is discovered that crater, built-up, cropland, and tea plantation contributed to heating the area, while pasture, shrub and forest area contributed to cooling the area.

## 7 ACKNOWLEDGEMENTS

The authors wish to thank Ecology Laboratory of School of Life Sciences and Technology ITB, BKSDA Jawa Barat, PT AIL Papandayan, and Iman Suryana for their support.

## 8 REFERENCES

Badan Geologi Kementerian ESDM. 2016. Penyelidikan Geokimia Gunung Papandayan, Jawa Barat (21 Mei-1 Juni 2016), Retrieved June 9, 2019, from http://merapi.bgl.esdm.go.id/pub/page.php?idx=209.

Barsi, J.A., Barker, J.L., Schott, J.R. 2003. "An Atmospheric Correction Parameter Calculator For A Single Thermal Band Earth-Sensing Instrument, Retrieved June 15, 2019, from https://atmcorr.gsfc.nasa.gov/.

BBKSDA Jabar. 2016. Informasi kawasan konservasi lingkup BBKSDA Jabar. Report BBKSDA Jabar, Indonesia.

Bonan, G. 2016. Ecological Climatology 3rd ed. Cambridge University Press, New York.

Carlson, T.N., Ripley, D.A. 1997. On the relation between NDVI, fractional vegetation cover, and leaf area index. Remote Sensing of Environment, 62(3), pp.241–252.

Dilekoğlu, M.F., Sakin, E. 2017. Effect of temperature and humidity in soil carbon dioxide emission. Journal of Animal and Plant Sciences, 27(5), pp.1596–1603.

Feizizadeh, B., Blaschke, T., Nazmfar, H., Akbari, E., Kohbanani, H.R. 2012. Monitoring land surface temperature relationship to land use/land cover from satellite imagery in Maraqeh County, Iran. Journal of Environmental Planning and Management, pp.1–26.

Forman, R. 2014. Urban Ecology. Cambridge University Press, Cambridge.

GCOS. 2016. The Global Observing System For Climate: Implementation Needs. Report GCOS-200, Guayaquil, Ecuador.

Hannah, L., Lovejoy, T., Schneider, S. 2005. Biodiversity and climate change in context. In: Climate Change and Biodiversity, edited by Lovejoy, T. & Hannah, L. Yale University, New Haven, pp. 3–14.

Hua, A.K., Ping, O.W. 2018. The Influence of land-use/land-cover changes on land surface temperature: a case study of Kuala Lumpur Metropolitan City. European Journal of Remote Sensing, 51(1), pp.1049–1069.
Jiménez-muñoz, J., Cristóbal, J., Sobrino, J.A., Sòria, G., Ninyerola, M., Pons, X. 2009. Revision of the single-channel algorithm for land surface temperature retrieval from Landsat thermal-infrared data. IEEE Transactions on Geoscience and Remote Sensing, 47(1), pp.339–349.
Kuenzer, C., Dech, S. 2013. Thermal Infrared Remote Sensing. Springer, Dordrecht.
Landis, J.R., Koch, G.G. 1977. The measurement of observer agreement for categorical data. Biometrics, 33, pp.159–174.
Latif, Z., Kamsan, M. 2017. Assessing the relationship of land use land cover on surface temperature in City of Shah Alam, Malaysia using Landsat-8 OLI. Journal of Fundamental and Applied Sciences, 9(5S), pp.514–525.
Lesado, A., James, A.J. 2018. Clay roofing tile : a cool roof ?. Open Journal of Science and Technology, 1(1), pp.6–8.
Loveland, T., Gallant, A., Vogelmann, J. 2005. Perspectives on The Use of Land-Cover Data for Ecological Investigations". In: Issues and Perspectives in Landscape Ecology, edited by Wiens, J. & Moss, M. Cambridge University Press, Cambridge, pp. 120–128.
Malbéteau, Y., Merlin, O., Gascoin, S., Gastellu, J.P., Mattar, C., Olivera-guerra, L., Khabba, S., Jarlan, L. 2017. Normalizing land surface temperature data for elevation and illumination effects in mountainous areas : A case study using ASTER data over a steep-sided valley in Morocco. Remote Sensing of Environment, 189, pp.25–39.
Mallick, J., Kant, Y., Bharath, B.D. 2008. Estimation of land surface temperature over Delhi using Landsat-7 ETM+. J. Ind. Geophys. Union., 12(3), pp.131–140.
Mbithi, D.M., Demessie, E.T., Kashiri, T. 2013. The impact of land use land cover ( LULC ) changes on land surface temperature ( LST ); a case study of Addis Ababa City , Ethiopia. In: Joint EUMETSAT/AMS Conference.
Pleim, J., McKeen, S. 2012. Meteorological processes affecting air quality – research and model development needs. EM Magazine - Air and Waste Management Association, 9, pp.52–55.
Primajati, M., Harto, A.B., Sulistyawati, E. 2011. Forest condition analysis based on forest canopy closure with remote sensing approach. Jurnal Biologi Indonesia, 7(1), pp.13–23.
Rao, V. 2014. Effects of urban heat island on air pollution concentrations. Int. J. Curr. Microbiol. App. Sci, 3(10), pp.388–400.
Sabins, F. 2007. Remote Sensing: Principles and Applications 3rd ed. Waveland Press, Long Grove.
Sobrino, J.A., Jiménez-muñoz, J.C., Sòria, G., Romaguera, M., Guanter, L., Moreno, J., Member, A., Plaza, A., Member, S., Martínez, P. 2008. Land surface emissivity retrieval from different VNIR and TIR Sensors. IEEE Transactions on Geoscience and Remote Sensing, 46(2), pp.316–327.
Stagl, J., Mayr, E., Koch, H., Hattermann, F., Huang, S. 2014. Effects of climate change on the hydrological cycle in central and eastern Europe. In: Managing Protected Areas in Central and Eastern Europe Under Climate Change, edited by Rannow, S. & Neubert, M. Springer, Dordrecht, pp. 31–43.
Sun, Q., Wu, Z., Tan, J. 2012. The relationship between land surface temperature and land use / land cover in Guangzhou , China. Environmental Earth Sciences, 65, pp.1687–1694.
Tang, H., Li, Z.-L. 2014. Quantitative Remote Sensing in Thermal Infrared: Theory and Applications. Springer, Heidelberg.
USGS. 2019. Landsat 8 (L8) Data Users Handbook 4th ed. USGS, Sioux Falls.
USGS. 2017. Landsat 8 OLI and TIRS Calibration Notices, Retrieved June 15, 2019, from https://www.usgs.gov/land-resources/nli/landsat/landsat-8-oli-and-tirs-calibration-notices.
Wang, Y., Liu, Y., Jin, J. 2018. Contrast effects of vegetation cover change on evapotranspiration during a revegetation period in the Poyang Lake Basin, China. Forests, 9(4), pp.1–14.
Zhou, W., Cao, F. 2019. Effects of spatial pattern of forest vegetation on urban cooling in a compact megacity. Forests, 10, pp.17–20.